



Science Arts & Métiers (SAM)

is an open access repository that collects the work of Arts et Métiers Institute of Technology researchers and makes it freely available over the web where possible.

This is an author-deposited version published in: <https://sam.ensam.eu>
Handle ID: <http://hdl.handle.net/10985/22095>

To cite this version :

Ahmed KTARI - Microstructure and mechanical property assessment of stainless steel-clad plate joint made by hybrid SMAW-GTAW multi-pass welding process - Welding in the World - 2022

Any correspondence concerning this service should be sent to the repository

Administrator : scienceouverte@ensam.eu



Microstructure and mechanical property assessment of stainless steel–clad plate joint made by hybrid SMAW-GTAW multi-pass welding process

Rami Ghorbel¹ · Ahmed Ktari^{1,2} · Nader Haddar¹

Abstract

The stainless clad steel plates (SCSPs) are used in several industrial fields such as petroleum and petrochemical industries due to their low cost and good corrosion resistance. In this work, the structural integrity assessment of a welded joint, produced by a hybrid SMAW/GTAW multi-pass welding process of SCSP, was carried out through non-destructive examinations, microstructural observations and mechanical characterization tests. The non-destructive examination showed that the welded zone is free from any sign of defect. The welded joint filled with ER316L revealed the presence of δ -ferrite, which was solidified as skeletal and lathy ferrite under ferritic-austenitic (FA) solidification mode. The microstructure of the weld metal transition zone (WM-TZ) filled with ER309L exhibited the presence of martensitic laths as well as a cellular and columnar structure. It was found that the diffusion of carbon element caused the forming of a decarburized layer in the substrate heat-affected zone (S-HAZ) during the welding process. The observation also revealed the presence of type I and type II boundaries along the fusion line, which are characterized by their martensitic nature. Based on the determination of the WM-TZ dilution percentage, which is equal to 32%, the presence of the martensite was also confirmed by Schaeffler diagram. The high micro-hardness values (~ 429 HV) and the low toughness (~ 22.9 J) measured respectively in vicinity of the WM-TZ also confirm the local hardening zone (LHZ) formed on the welded zone after bending tests.

Keywords Stainless clad steel · Multi-pass welding · Mechanical properties · Microstructure · Transition zone · Local hardening zone

Abbreviations

SCSP	Stainless clad steel plate
SMAW	Shielded metal arc welding
GTAW	Gas tungsten arc welding
SAW	Submerged arc welding
NDE	Non-destructive examination
WM	Weld metal
HAZ	Heat affected zone
WM-CL	Weld metal clad layer
WM-TZ	Weld metal transition zone

BM-S	Base metal substrate
WM-S	Weld metal substrate
S-HAZ	Substrate heat-affected zone
BM-CL	Base metal clad layer
LHZ	Local hardening zone
FB	Fusion Boundary

1 Introduction

Stainless clad steel plate (SCSP) is a composite structural bi-material made of a stainless steel as a cladding layer and carbon steel as a substrate. It is commonly manufactured by using explosion welding [1], weld overlay [2], roll bonding [3] and other welding processes [4, 5]. Compared with pure stainless-steel plate, the SCSP not only combines the advantages of the two component materials, such as excellent corrosion resistance, high mechanical properties and good environmental stability, but may also balance the cost. Actually, the use of the low carbon steel as a substrate can

Recommended for publication by Commission XI - Pressure Vessels, Boilers, and Pipelines

✉ Rami Ghorbel
rami.ghorbel@enis.tn

- ¹ Laboratoire Génie des Matériaux et Environnement, ENIS, Université de Sfax, B.P.1173, 3038 Sfax, Tunisia
- ² MSMP-EA7350, Arts et Métiers ParisTech, 2 cours des Arts et Métiers, 13617 Aix-en-Provence, France

reduce the amount of alloy elements like chromium (Cr) and nickel (Ni) by 70–80% [6]. Considering those advantages, the SCSP has become, in the last few years, an interesting alternative to ordinary pure stainless-steel plates in many industrial applications such as petroleum, petrochemical and pressure vessel industries [7–9].

Several welding processes, such as shield metal arc welding (SMAW) [10, 11], submerged arc welding (SAW) [12], gas tungsten arc welding (GTAW) [13, 14] and laser welding [15], are suitable for joining SCSP. However, the differences in chemical compositions and physical properties between the carbon steel and stainless steel make the welding of the SCSP relatively difficult [10]. The base material mismatching between the clad layer and the substrate may lead to the generation of a high discontinuous residual stress at the interface between them after welding process [16]. In addition, Cr and Ni alloy elements in the WM-CL can easily dilute and diffuse into the WM-S, leading to low contents of alloy elements and a low corrosion resistance of the WM-CL as well as a disappearance of the δ -ferrite in the vicinity of the WM-CL interface [17]. Meanwhile, Wang et al. [18] reported in their work that a decarburized layer and a carbon-rich layer were also found in the welding interface due to the easy dilution and the carbon diffusion. Furthermore, the excessive diffusion of alloying elements can result in the formation of Cr_{23}C_6 carbides at the welding interface, leading to a severe inter-granular depletion (Cr-depletion) and inter-granular cracks [8].

In case of the SCSP, the preparation of the coupon test prior to welding (i.e., the groove shape) and the selection of the suitable welding sequences are crucial. These preparations may affect the mechanical properties of the SCSP welded joint. Hence, in order to satisfy the requirements in terms of mechanical properties and to ensure a good welding quality, some researchers studied the influence of different groove shapes on the mechanical behaviour and microstructure of the SCSP welded joint [10–13]. While other researchers investigated the effect of the welding sequences on microstructure and mechanical properties of the SCSP welded joint [10–19], Li et al. [13] have studied, firstly, the weld joint performance of the L415/316L clad steel pipes using four groove shapes. Then, they investigated its microstructures, mechanical properties and corrosion resistances. The results of this paper showed that the U-V shape, with an angle of 60° on the V-shape and with 1 mm as a blunt edge, is the most suitable configuration between the studied four groove shapes. Dhib et al. [10] have studied the weld performance of the A283 Gr C/A240 TP316L SCSP using two groove shapes (V-shape and U-V shape). Then, they investigated its mechanical properties. Results showed that failure occurred when they performed the bending test on the V-shape configuration (first configuration). In addition to

that, impact toughness of the V-shape configuration was found below the standard requirement ($< 27 \text{ J}$). The same authors have also investigated the weld joint performance of the same SCSP (A283 Gr C/A240 TP 316L) using U-V shape and applying two different welding sequences. Results showed that the toughness of the second configuration is below the standard requirement. Moreover, the highest micro-hardness values were observed on the WM-TZ of the second configuration. Results thereby show that proceeding by welding, the parent metal using E7018 followed by welding the transition phase using the ER309L and finishing by welding the clad layer using ER316L (third configuration) hereby improves the welding efficiency of the welded joint. Similar findings were reported by Yu et al. [19] when they investigated the mechanical properties of the SCSP (Q235/SUS304). These authors concluded that welding the clad layer without using the transition phase affects not only the microstructure (excessive diffusion of Ni and Cr) but also the corrosion resistance and mechanical properties. Based on the above discussion, it is clearly seen that the weld joint microstructures and their corresponding mechanical properties are highly dependent on multi-pass welding process parameters and configurations. However, in addition, the microstructure morphology of a welded joint is highly affected by solidification parameters. Thus, it is useful to understand well the relationship that exists between the different weld pool solidification parameters (viz. growth rate R , temperature gradient G , and undercooling ΔT and the resulting microstructure). David et al. [20, 21] have reported that solidification parameters G and R are important in combined forms $G \times R$ and G/R since they influence respectively the scale of the solidification morphology and the sub-structure of the weld metal. Trivedi et al. [22] have reported that the solidification front presents a planar character along the fusion line since the ratio G/R is maximal and transforms to cellular and columnar when moving towards the weld centreline (i.e. G/R decreases). Bunaziv et al. [23] have explained that along the fusion line, where the G is largest and the R is smallest, the criterion for plane front stability $(G_L/R) > (\Delta T_0/D_L)$, where G_L is the thermal gradient in the liquid, D_L is the solute diffusion coefficient in the liquid and ΔT_0 is the equilibrium solidification temperature range, is most easily satisfied leading to the presence of a planar structure. They have also explained that throwing the weld centreline, G decreases and R increases promoting therefore a planar instability which gives rise to a cellular and then columnar structure.

In harmony with the above discussed studies and based on the third weld configuration studied by Dhib et al. [10], a new hybrid SMAW/GTAW multi-pass welding configuration was proposed and realized in our previous

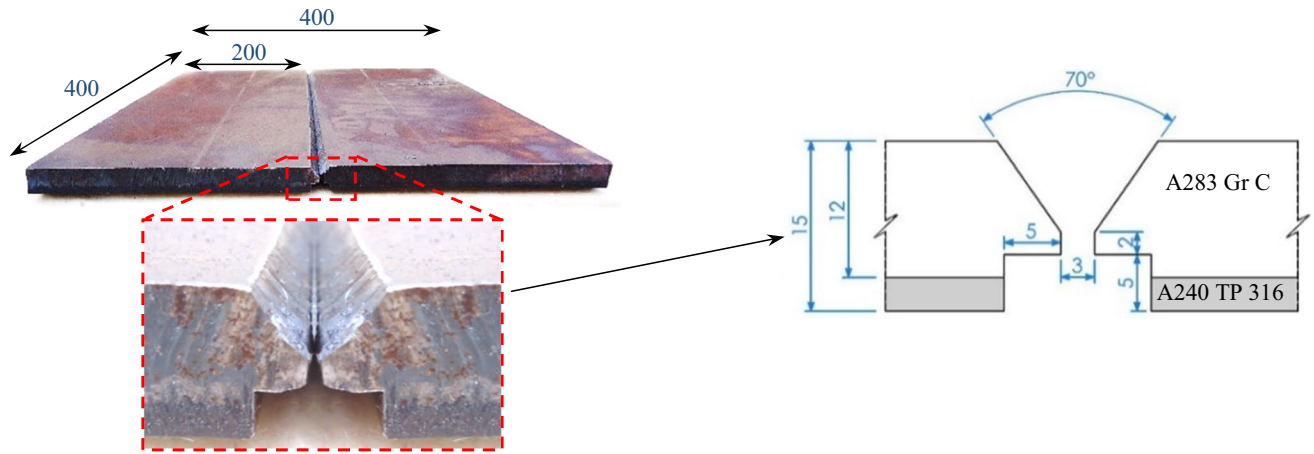


Fig. 1 Form and dimensions of the prepared plates and the butt-weld U-V shape for welding process

Table 1 Chemical composition of the SCSP and filler metals (wt. %)

	Elements	C	Si	Mn	P	S	Cr	Ni	Mo
Base material	A283 Gr C	0.167	0.172	0.479	0.019	0.022	–	–	–
	A240 TP 316	0.017	0.514	1.124	0.038	0.002	16.654	10.109	2.092
Filler metals	ER 316L	0.08	0.53	1.17	0.053	0.008	16.18	10.55	1.90
	E7018	0.23	0.171	0.402	0.032	0.012	0.024	0.021	< 0.002
	ER 309L	0.025	0.45	1.8	0.02	0.02	24	13	–

work [24] to join the SCSP in order to reduce the number of passes and consequently the welding time and cost. The authors have focalized in the first part of their study the effect of the generated heat flux during the multi-pass welding process on the angular distortion and the longitudinal shrinkage of the SCSP welded joint [24]. Preliminary investigation of the weld mechanical performances including tensile and bend tests showed that the welded joint has higher mechanical tensile strength than the parent metal and that no separations, fractures or tearing appeared on the specimen surface after the bending test. However, the bend specimen showed the presence of a bulging phenomenon located on the welded joint bent surfaces that was explained by the presence of a low hardening zone (LHZ) with low plasticity.

Hence, our previous research [24] was limited on evaluating the welded joint performances using only conventional tensile and bend tests, which is insufficient to understand the main cause leading to the LHZ apparition. It is useful to further investigate the structural integrity of the welded joint in order to (i) identify the different microstructures within the SCSP-welded joint produced by multi pass SMAW/GTAW process and (ii) understand the relationships that exist between the observed microstructure and the resulting mechanical properties of the

welded joint in order to better understand the origin of the LHZ phenomenon.

2 Materials and methods

2.1 Base and fillers materials

Two plates with dimensions of 200 mm × 400 mm were extracted from a clad sheet metal obtained by a hot-roll bonding of a 12-mm low carbon steel (A 283 Gr C) and a 3-mm austenitic stainless steel clad layer (A 240 TP 316L). The dimensional details of the test coupon are given in Fig. 1. The chemical composition and the monotonic mechanical properties of the SCSP base material studied in this work are given respectively in Tables 1 and 2.

Table 2 Mechanical properties of the SCSP (A283 Gr C + A240 TP316L) at room temperature

Tensile strength	<i>R_m</i> (MPa)	438
Yield strength	<i>R_e</i> (MPa)	418
Young's modulus	<i>E</i> (GPa)	210
Poisson's ratio	<i>ν</i>	0.3
Elongation	<i>A</i> (%)	30

Table 3 Multi-pass welding process parameters used for joining the studied material

Weld pass No.	Filler metal	Filler metal Ø (mm)	Current and polarity	Current (A)	Voltage (V)	Welding speed (mm/s)	Heat input (kJ/mm)
1	E7018	2.5	DCRP*	85	22	1.43	1.31
2	E7018	3.2	DCRP	116	22	1.13	2.27
3	E7018	3.2	DCRP	113	24	1.86	1.46
4	ER309 L	2.4	DCSP**	133	10	1.3	1.02
5	ER309 L	2.4	DCSP	141	11	1.18	1.31
6	ER316 L	2.4	DCSP	142	11	1.1	1.42
7	ER316 L	2.4	DCSP	140	11	0.93	1.66
8	ER316 L	2.4	DCSP	130	10	1.25	1.04
9	ER316 L	2.4	DCSP	133	10	0.86	1.55

DCRP direct current reverse polarity, *DCSP* direct current straight polarity

2.2 Welding procedure

In this study, the welding process was carried out using three filler metals E7018, ER316L and ER309L to join the low carbon steel (A283 Gr C), austenitic stainless steel (A 240 TP 316L) and the transition zone, respectively. Typical chemical compositions of these filler metals are given in Table 1. Three passes on the carbon steel side were performed using the SMAW process whereas two passes in a transition phase and four passes on the stainless-steel side using both GTAW process. The used filler metal for each pass and its corresponding welding parameters are given in Table 3. For more details concerning the welding process, see Ref. [24].

2.3 Welded joint characterization

2.3.1 NDE

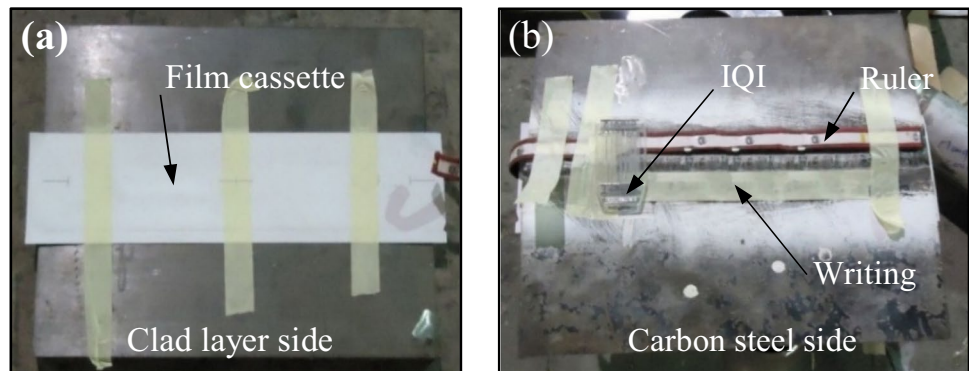
In order to confirm the welded joint integrity, several non-destructive examination (NDE) tests were performed to detect the presence of somewhat surface and/or volume defects. Indeed, a visual examination, a dye pen examination in the stainless-steel side, a magnetic practical

examination in the carbon steel side and a radiographic examination (Fig. 2) were carried out according to ASME code [25] (Section IX QW-302.2).

2.3.2 Micro- and macrostructural analyses

A specimen, with dimensions of $120 \times 15 \times 9.5$ mm, was used to perform micro, macro-graphic and micro-hardness examinations. Both sides of the specimen were mechanically polished using SiC grits papers with a grit number varying from 280 to 1200, followed by a final polishing using 6-, 3- and 1- μ m diamond pastes, respectively. The specimen sides were differently etched. The first side was chemically etched, at room temperature, using iron chloride in order to reveal the macrostructure of the welded joint. The second one was prepared in order to examine the welded joint microstructure. For the second specimen side, the carbon steel was chemically etched using 3% of the nitric acid alcohol solution for 5 s while the austenitic stainless steel was electrolytically etched using 10% of the oxalic acid solution in distilled water at 6 V for 20 s. The microstructure of the welded joint was investigated using LEICA® metallographic microscope.

Fig. 2 Setting up the radiographic test coupon; **a** the film cassette on stainless steel side and **b** the IQI, ruler and writing on the carbon steel side



2.3.3 Mechanical characterization setup

In order to characterize the mechanical properties of the joint, several specimens were cut from the welded coupon. Specimens were extracted, from the test coupon using water jet as shown in Fig. 3 and then machined in order to obtain the required dimensions according to the ASME IX code [25]. Tensile and bend tests were carried out, at room temperature, to confirm the reliability of the welded joint as described in ref. [24]. In addition to tensile and bend tests, toughness and micro-hardness experiments were deeply investigated in this work in order to check the integrity of the joint under dynamic Charpy impact test and correlates mechanical properties to microstructural observations. Indeed, toughness specimens were notched using V-Notch cutter Machine in the WM and the HAZ, respectively, as shown in Fig. 3c. Then, they were placed into a LR-cdw-60@ low temperature-testing machine until they reached the temperature of $-29\text{ }^{\circ}\text{C}$. This temperature was fixed since it corresponds to the operating temperature of containers dedicated to acid conditioning. Charpy tests were performed using JB-W300A@ impact testing machine. The absorbed energies were measured, and the fractured surfaces were investigated.

Given the expected complexity of the microstructure in the welded joint, since it presents the assembly

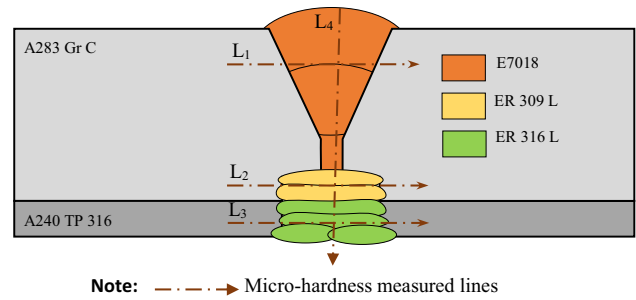


Fig. 4 Micro-hardness measurement paths on the welded specimen

of a be-material with three different filler metals, several micro-hardness measurements were carried out on the weld zone, along four different paths, as depicted in Fig. 4. The micro-hardness tests were conducted with Innova® testing machine, using Vickers indenter under a load of 0.1 kg.

3 Results and discussions

3.1 A preliminary study

The welded joint has shown a good visual appearance. Besides, no defects were detected after performing the

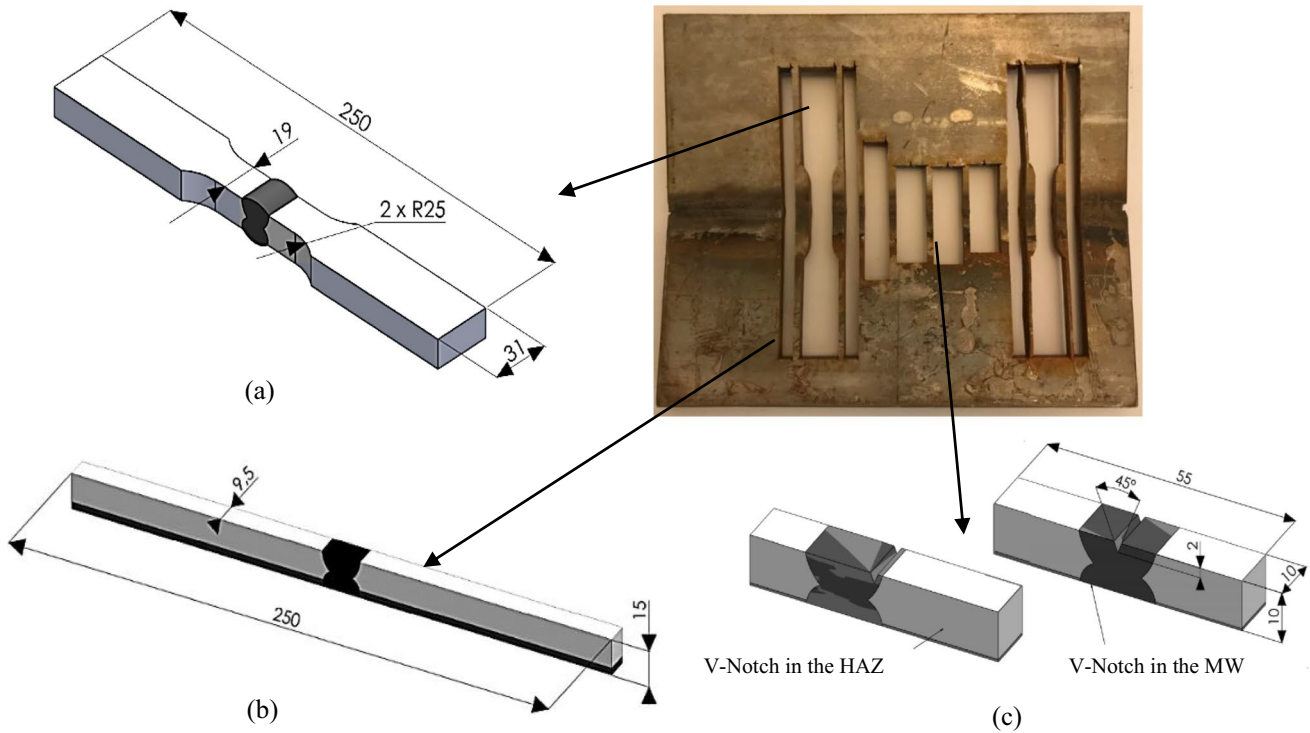


Fig. 3 Form and dimensions (in mm) of specimens extracted from the welded plates. **a** Tensile test specimen. **b** Bend test specimen. **c** Impact test specimen

Fig. 5 Radiographic film of the welded joint

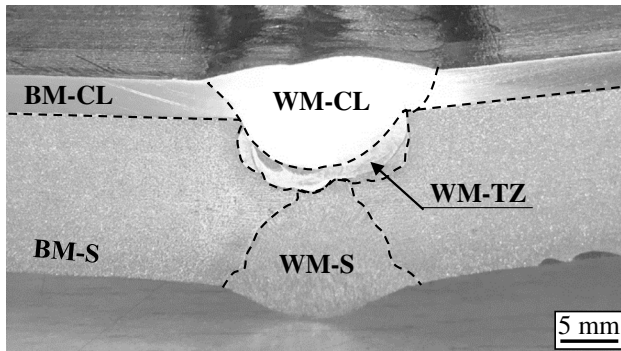
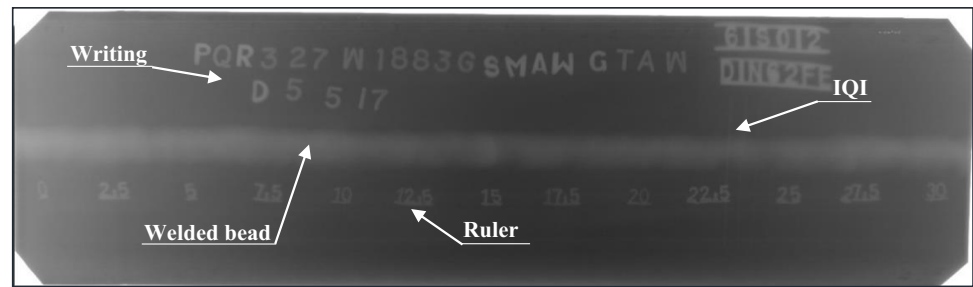


Fig. 6 Macroscopic observation of the welded joint

dye pen and magnetic practical examinations. Regarding the radiographic examination, the film revealed a full weld penetration with a complete sidewall fusion as illustrated in Fig. 5. Likewise, the film revealed a welded bead free of any sign of defects.

The weld cross section was examined after being etched. Figure 6 reveals the presence of three different zones in the welded joint as follows: the WM-S, the WM-CL and the WM-TZ. In addition to that, the welded joint, shown in this figure, exhibits a full weld penetration with a homogeneous fusion weld in the carbon steel side, stainless steel side and in the transition side. Likewise, the examination of the welded joint and the extent of the HAZ revealed the exemption of any sign of discontinuities or defects, which confirms the obtained NDE results.

3.2 Microstructural analysis

In this contribution, a meticulous microstructural investigation of the welded joint was carried out in order to recognise the different phases presented in Fig. 6 as well as their interfaces. The microscopic observations, shown in Figs. 7, 8, 9, 10, 11, 12, 13, 14, revealed the presence of a heterogeneous microstructure resulting from the generation of a chemical and temperature gradient during the welding process [26]. In this study, given the complexity of the microstructure that composed the welded zone, the microstructure analyses of

the joint are performed in three levels viz: carbon steel side, clad stainless steel side and transition zone.

3.2.1 Carbon steel welded joint side

The microstructure evolution across the welded joint filled with E7018 is shown in Fig. 7. The microstructure of the BM-S is composed of pearlite (dark grains) and ferrite (bright grains) phases (Fig. 7a). In addition, Fig. 7 reveals that pearlitic grains become finer while going from the BM-S zone to the WM-S zone (Fig. 7c) passing through the S-HAZ zone (Fig. 7b). Similar findings were observed by Dhib et al. [10] when they studied the metallurgical properties of the SCSP A283 Gr C/A240 TP 316L after welding. In addition, Fig. 7 shows that the microstructure of the carbon steel welded joint side exhibits a typical and healthy structure without any sign of martensitic phase.

3.2.2 Stainless-steel welded joint side

The microstructure of the welded joint zone filled with ER316L is shown in Fig. 8. The examination of the BM-CL reveals the presence of a largely austenitic (γ - white) structure with the presence of some twins (Fig. 8a). Not far from the BM-CL, the microstructure observed along the fusion line shows that the crystallization occurred according to an epitaxial mode (Fig. 8b). Indeed, the solidification growth occurs by arranging atoms in the liquid phase on the existing BM-CL crystal-line, thus extending it without altering the original crystallographic orientation. As a result, grain boundaries from the BM-CL are continuous across the fusion line, forming solidification grain boundaries in the WM-CL [8, 27, 28]. Far away from the fusion line, the microstructure of the WM-CL (Fig. 8c) presents an austenite matrix with a dendritic δ -ferrite, which mainly solidified in skeletal and lathy morphologies. This type of microstructure depends on the WM-CL solidification mode. The skeletal and lathy morphology of the δ -ferrite theoretically depends on the solidification rate of the WM-CL, which is mainly controlled by the diffusion of the Cr and Ni [29]. Indeed, and

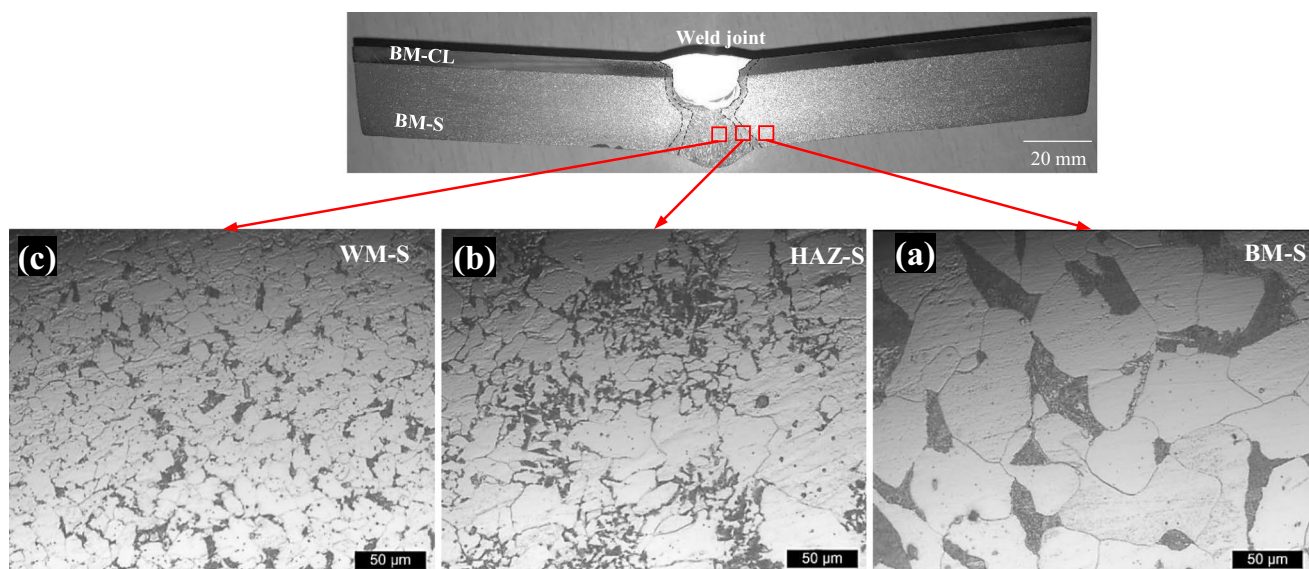


Fig. 7 Metallographic examination of welded joint (the carbon steel side). (a) Base Metal Substrate (b) Heat Affected Zone Substrate (c) Weld Metal Substrate

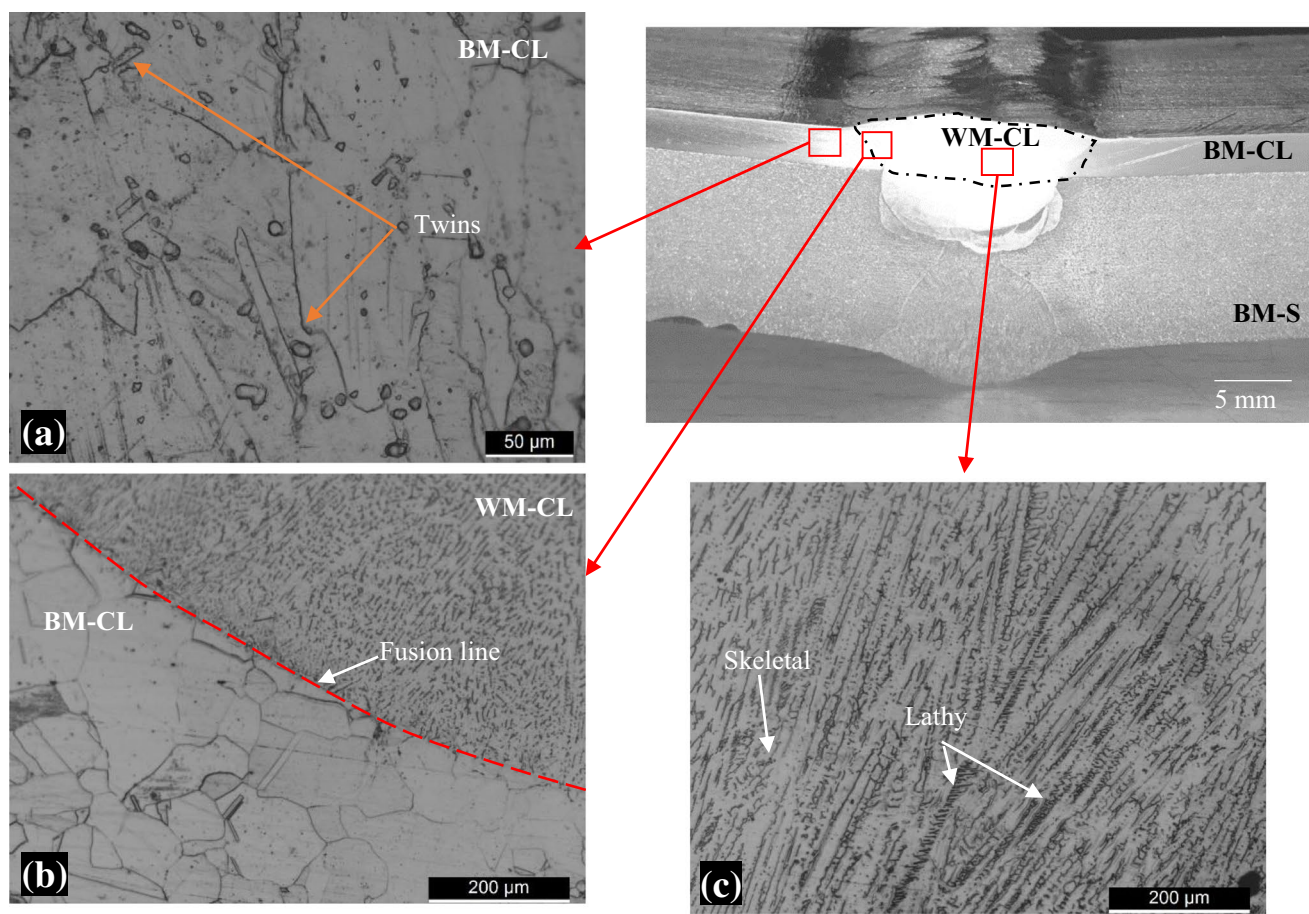


Fig. 8 Metallographic examination details of stainless-steel side. (a) Base Metal Clad Layer (b) Fusion line between Base Metal Clad Layer/ Weld Metal Clad Layer (c) Weld Metal Clad Layer

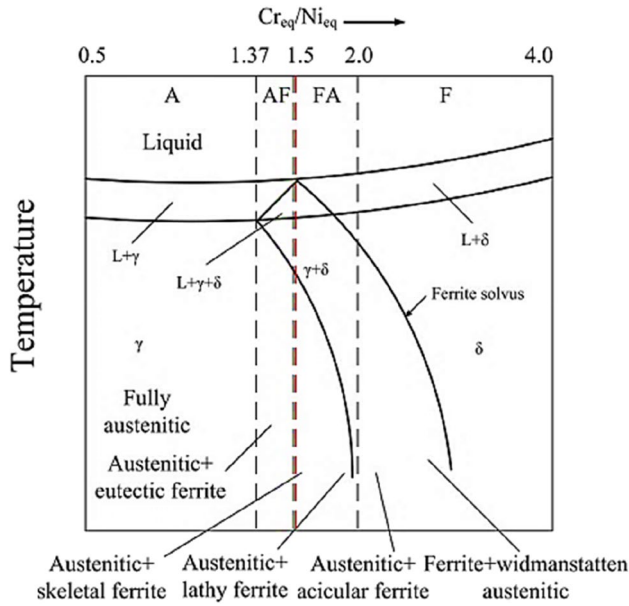


Fig. 9 Solidification modes of austenitic stainless steels based on different Cr_{eq}/Ni_{eq} values [29]

based on Fig. 9, the solidification mode of the WM-CL depends on the ratio of the equivalent chrome $[Cr]_{eq}$ and equivalent nickel $[Ni]_{eq}$, expressed as follows:

$$[Cr]_{eq} = \%Cr + \%Mo + 1.5\%Si + 0.5\%Nb \quad (1)$$

$$[Ni]_{eq} = \%Ni + 30\%C + 0.5\%Mn \quad (2)$$

In order to calculate the percentage of $[Cr]_{eq}$ and $[Ni]_{eq}$ in WM-CL zone, a spark optical emission spectroscopy (OES) technique was used to determine the chemical composition of this zone. The found result is summarised in Table 4.

According to Fig. 9, the solidification mode of the WM-CL zone is a primary ferritic solidification, with ferrite to austenite formation (FA mode). Chassignole [30] reported that the δ -ferrite, in the FA solidification mode, crystallizes at first. Then, the $\delta \rightarrow \gamma$ transformation occurs during the cooling process. Since this transformation is incomplete,

the residual δ -ferrite remains in the WM-CL after solidification.

Idem with the observations shown on the carbon steel welded joint side, the microstructure of the stainless steel welded joint side reveals a healthy structure without any sign of martensitic phase.

3.2.3 Transition phase welded joint

In this section, the microstructure evolution of the welded joint zone filled with ER309L is investigated (Fig. 10). Figure 10a reveals that the S-HAZ microstructure is almost pearlitic with a predominant appearance of ferrite coarse grains located at the S-HAZ adjacent to the WM-TZ. The disappearance of the pearlitic grains may be ascribed to the carbon depletion, which occurs during the welding process. Li et al. [6] reported in their study that due to the element diffusion, a decarburized layer is formed in the S-HAZ and the precipitated carbon is aggregated along the fusion line. The appearance of the ferrite coarse grains may be attributed to the grain coarsening behaviour under the effect of high temperature generated during the welding process, as reported by An et al. [8]. In analogy with the bonding phenomenon that occurs, at high temperature, between the clad layer and the substrate, Dhib et al. [31] reported in their work that carbon element can easily migrate from BM-S forwards BM-CL due to the high mobility of its small atomic radius (0.077 nm). The same authors have also reported that grain coarsening and decarburization have occurred at the BM-S near the interface due to long exposure time at high temperature.

The same phenomena were also observed in Fig. 10b while examining the WM-S/WM-TZ interface. The layer thickness of coarse grains located at WM-S/WM-TZ interface exhibits an average value of $55 \pm 7 \mu m$, which is smaller than that located at the S-HAZ/WM-TZ interface (average of $75 \pm 6 \mu m$) (Fig. 10a). The difference in the layer thickness values can be explained by the difference in carbon percentage between A283 Gr C (C (wt %) = 0.167) and E7018 (C (wt %) = 0.23). Indeed, during the welding, a decarburization of the S-HAZ and the WM-S occurs until the WM-TZ reaches its nominal carbon content. Since E7018 has high carbon content, the carbon depletion in the WM-S near the interface will occur with a small width of the decarburized

Table 4 Chemical composition of the WM-CL (wt. %) and $[Cr]_{eq}/[Ni]_{eq}$ ratio

Element	C	Si	Mn	Cr	Ni	Mo	Nb	$[Cr]_{eq}$	$[Ni]_{eq}$	$[Cr]_{eq}/[Ni]_{eq}$
WM-CL (analysed zone)	0.053	0.333	2.41	19.48	11.43	1.61	0.057	21.637	14.225	1.52
BM-S	0.167	0.172	0.479	—	—	—	—	0.26	5.25	—
ER309L	0.025	0.45	1.8	24	13	—	—	24.68	14.65	—

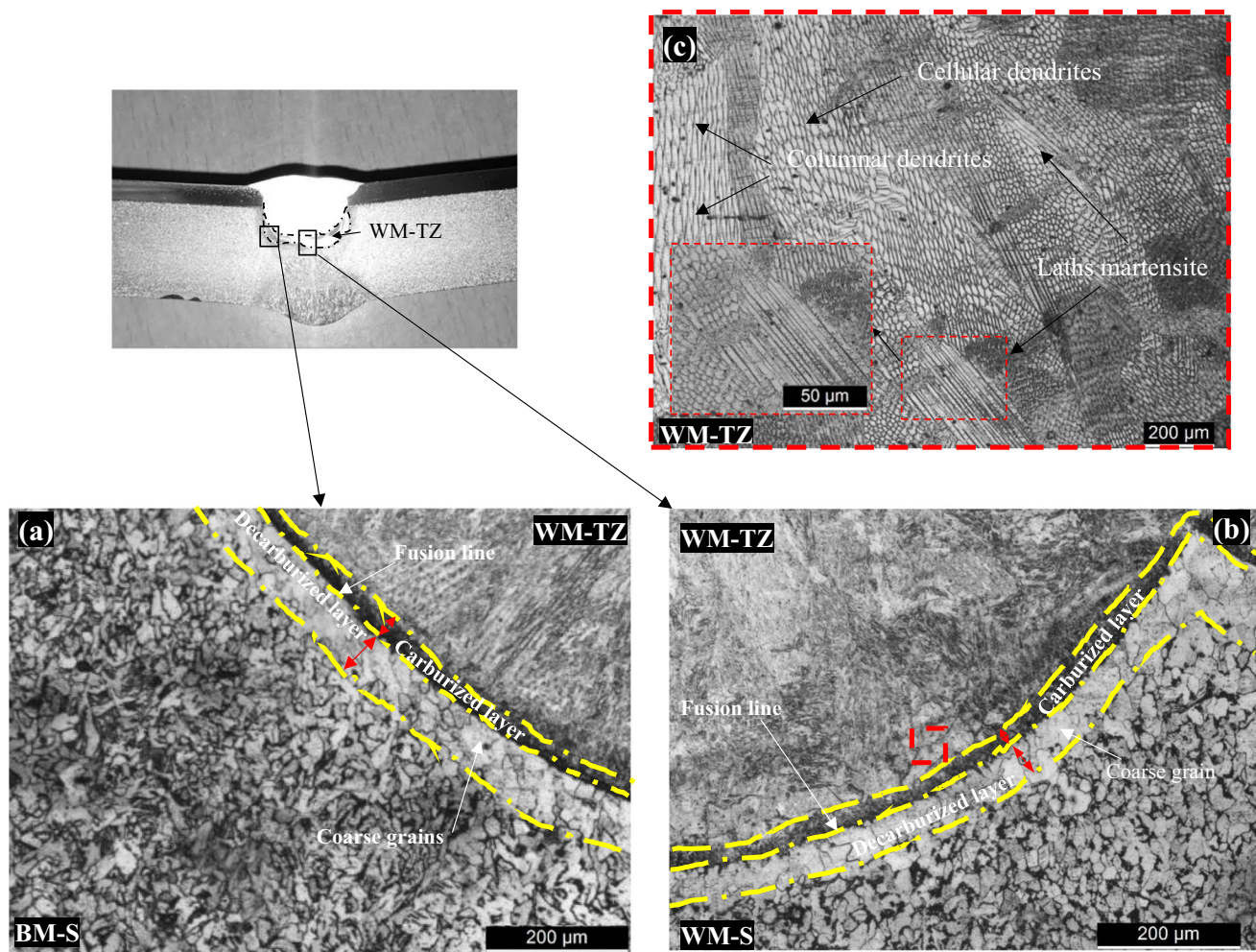


Fig. 10 Metallographic examination of the weld metal transition zone. (a) Weld Metal Transition Zone/ Base Metal Substrate interface (b) Weld Metal Transition Zone/ Weld Metal Substrate interface (c) Weld Metal Transition Zone

layer. Figure 10a and b also reveal the presence of a dark layer $25 \pm 3 \mu\text{m}$ wide. Due to the excessive diffusion of the carbon element from BM-S and WM-S zones to WM-TZ, a carbon-rich layer with a dark aspect called carburized layer is observed [8]. The comparison between thickness values of carburized and decarburized layers shows that the decarburized layer is always thicker than the carburized layer. This result may be attributed to the difference of diffusion velocities and the carbon element solubility in austenite and ferrite phases [8]. Actually, the carbon diffusion can be easily pronounced thanks to its small atomic radius (0.077 nm), which offers it great mobility. In addition, the microstructure of the WM-TZ shown in Fig. 10c revealed the presence of martensitic laths and cellular and columnar sub-grains elongated according to their local solidification direction. The microstructure of the WM-TZ has undergone several complex thermophysical phenomena, during the multi-pass welding process, which are related to the re-melting and solidification of the welded pool. The grain morphology

transformations are due to the combined effects of both temperature gradients (G) and the rate of grain's growth (R) generated during the solidification process. The effect of the temperature gradient G and the growth rate R on the morphology and the size of the solidified microstructure is represented in Fig. 11. When carrying out the subsequent pass with ER309L, a molten pool will be formed and then solidified. Since the ratio G/R is maximal at the bottom of the molten pool (i.e., near the fusion boundary), there will be few planar crystals that firstly form. With the movement of the solid/liquid interface towards the weld pool centreline, the solidified microstructure progressively changes from planar crystals to cellular and then to columnar due to the decrease of the ratio G/R . The same result was confirmed by Li et al. [32] when they studied the microstructure and mechanical property evolution of multipass laser welding. These authors have also reported that when the bottom of the molten pool is being solidified, the top of this molten pool is also being solidified into dendrite direction because of the

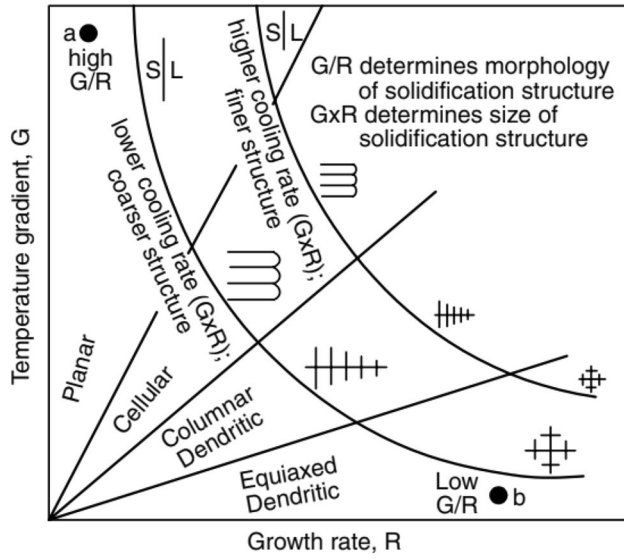


Fig. 11 Effect of temperature gradient G and growth rate R on the morphology and size of solidification microstructure [34]

change in G direction under the effect of the natural convection. However, since the solidification rate from the bottom to surface is much faster than that from surface to bottom, the columnar d accounts for a large area in the welded bead. The same authors [32] have also reported that the effect of the multi-pass welding has not only affected the microstructure but also the mechanical properties of the welded joint. Rathod et al. [33] reported in their work that the cellular and columnar structures are characterized by their martensitic nature that can affect the mechanical properties of the weld.

In order to confirm the observed microstructure, it is useful to predict which phase is present in the WM-TZ zone using Schaeffler diagram as previously explained. However, in our case study, OES analysis cannot be performed to determine the chemical composition the WM-TZ zone given its small cross-section area compared to dimensions of sparking area. For this, another technique was used to predict the presence of the martensitic structure. $[\text{Cr}]_{\text{eq}}$ and $[\text{Ni}]_{\text{eq}}$ of respectively A 283 Gr C and ER309L were calculated (Table 4) and plotted on the Schaeffler diagram, as shown in Fig. 12. According to this diagram, the martensite-austenite mixed zone can be formed in regions where the dilution ratio is between 31 and 53%. For this, the dilution was then calculated basing on the macro-graphic cross section shown in Fig. 6. The dilution can be defined as the contribution of the BM-S into the WM-TZ (Fig. 13). The dilution was calculated using Eq. 3, the dilution's value was found 32%, and the presence of a martensitic structure is confirmed (Fig. 12).

$$\% \text{dilution} = \frac{a + b + c}{a + b + c + d} \times 100 \quad (3)$$

The fusion boundary (FB) in the vicinity of the carburized layer (i.e. between the WM-TZ and the BM-S) was evaluated. A type-II boundary running parallel to the FB is found in the WM-TZ, as shown in Fig. 14. This type-II boundary parallels the fusion boundary approximately 40 μm away from the WM-TZ. Type II boundaries may be a result from a change in the primary mode of solidification. Actually, the primary solidification occurs as a ferrite (bcc) in the S-HAZ and as an austenite in the WM-TZ. At

Fig. 12 Schaeffler diagram [29]

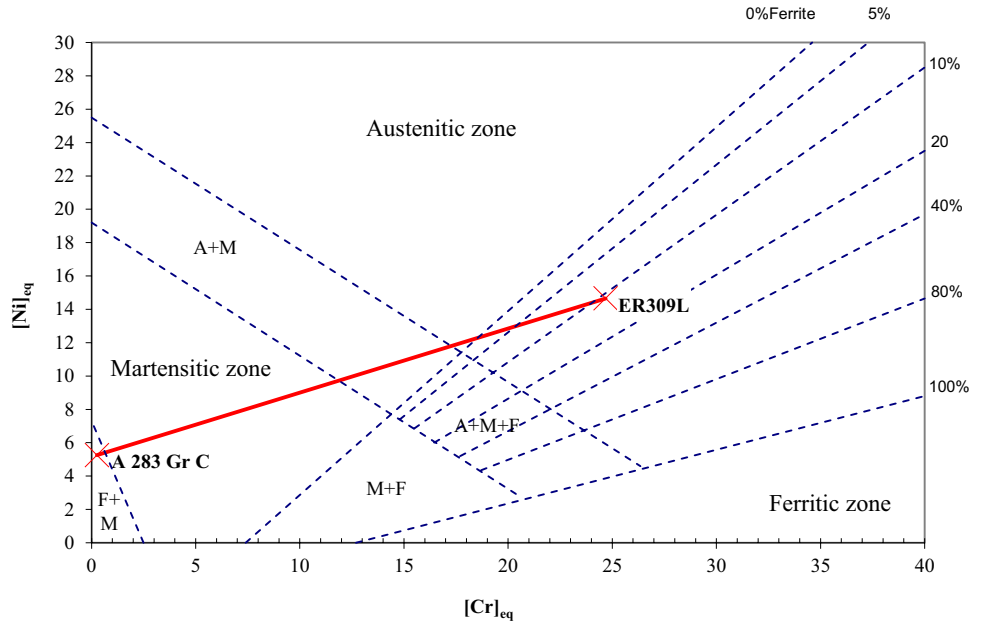


Fig. 13 Schematic view showing the calculation of dilution in a fusion weld

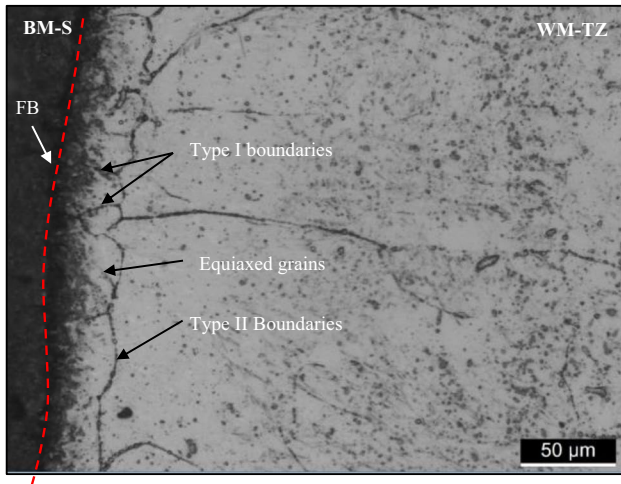
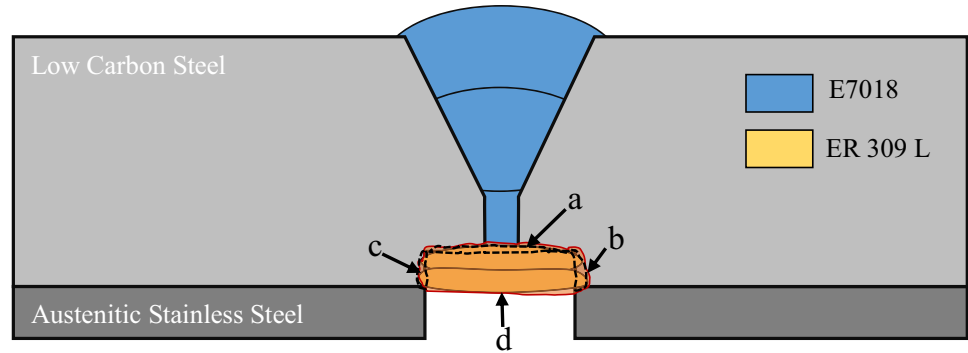


Fig. 14 Metallographic examination of the fusion boundary in BM-S/WM-TZ

high temperature, the S-HAZ will undergo an allotropic δ - γ transformation. The fusion line becomes, therefore, an austenite (fcc) boundary between the S-HAZ (fcc) and the WM-TZ (also fcc) in the austenitic temperature range. Since both sides have an austenitic lattice, the austenitic boundary can migrate easily into the WM-TZ. This migration is principally the result of the composition gradients within the transition region between the S-HAZ and the WM-TZ. [35, 36].

Several researchers prove the formation of a martensitic structure in the type-II boundary. Rowe et al. [37] reported in their study that the intermediate composition along the drawn line on the Schaeffler diagram (i.e. between ER309L and A 283 Gr C) would develop martensitic and austenitic plus martensitic microstructures. Nelson et al. [38] prove that if the dilution is between 20 and 80%, the microstructure of the WM-TZ will be observed as a mostly austenitic microstructure with a band of martensite along the FB. Based on the above discussion, we can conclude that the microstructure of the type-II boundaries is a martensitic structure since the dilution is 32%. Furthermore, type-I boundaries, running

roughly perpendicular to the FB between the equiaxed grains as a result of an epitaxial growth, have also been found [37].

3.3 Mechanical characterization

3.3.1 Micro-hardness

The micro-hardness measurements conducted along four paths on the welded specimen (Fig. 4) are depicted in Fig. 15. The micro-hardness profile performed along L1 direction (Fig. 15a) shows that the hardness values measured on the S-HAZ surface (average 208 ± 8 HV) are slightly higher than those measured on the WM-S (average 213 ± 5 HV) and the BM-S (average 171 ± 9 HV). The highest micro-hardness level measured on the S-HAZ can be ascribed to the perlite dissociation, which is observed in Fig. 7b. In contrast, the micro-hardness values measured on the WM-S are lower, but still higher than those measured on the BM-S owing to the high cooling rate and grain refinement at the WM-S (Fig. 7c).

Figure 15b displays the micro-hardness profile of the welded joint along L2 direction. It is obvious that micro-hardness values measured on the S-HAZ near the interface (average 429 ± 30 HV) are significantly higher than those measured on the WM-TZ (average 384 ± 14 HV) and the BM-S (average 171 ± 17 HV). The highest micro-hardness level measured on the S-HAZ can be assigned to the carburized layer shown in Fig. 10a along the FB. Herein, it is obviously clear from Figure 15b that the highest micro-hardness values are in the vicinity of the fusion line. Indeed, the carbide forms in this area due to the chrome and carbon diffusion phenomenon at high temperature leading to the formation of the type I and type II boundaries as clearly seen in Fig. 14. However, the micro-hardness values measured on the WM-TZ are lower, but still higher than those measured on the BM-S. This can be ascribed to the presence of the martensite laths as already observed in Figure 10c.

Figure 15c shows the micro-hardness curve across the L3. The micro-hardness values measured on the WM-CL vary slightly (average 221 ± 19 HV) and are found to be

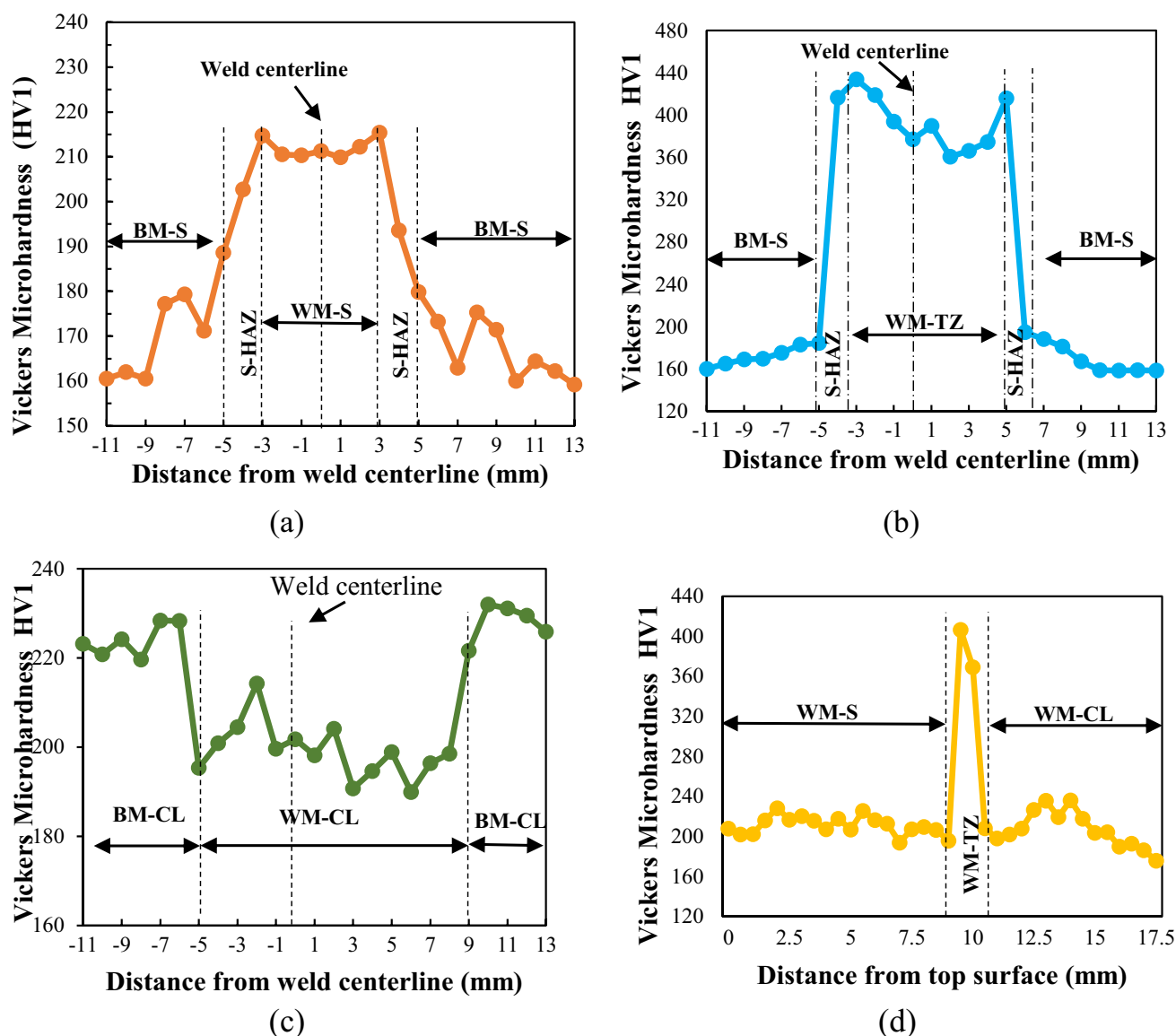


Fig. 15 Micro-hardness of the welded joint along: **a** L1, **b** L2, **c** L3 and **d** L4 profiles

similar to the BM-CL. The reason of this slight variation can be explained by the variation of microstructures between BM-CL and WM-CL as shown in Figure 8b.

The micro-hardness profile along L4 direction is shown in Fig. 15d. It is clear that both of WM-CL and WM-S have shown no large variation in micro-hardness values. In contrast, the micro-hardness value of the WM-TZ increased significantly and reached about 406 HV. This can be attributed to the presence of the martensitic phase previously observed in Fig. 10c as well as the presence of the carbide agglomerated in the FB and observed as type I and type II boundaries (Fig. 14).

On the bases of the previous discussion, the hardening zone shown in the WM-TZ and its S-HAZ are confirmed not only by the presence of the martensitic phase but also by the

carburation/decarburation phenomena, which accelerate the formation of the chromium carbide leading thereafter to a hardening at the WM-TZ/S-HAZ interface. This hardening zone may adversely affect the bend test and impact toughness properties of the welded joint due to the inhomogeneity.

3.3.2 Tensile and bend test

The transverse tensile strength specimens have been evaluated in our previous investigation [24]. The main results are summarized in Table 5.

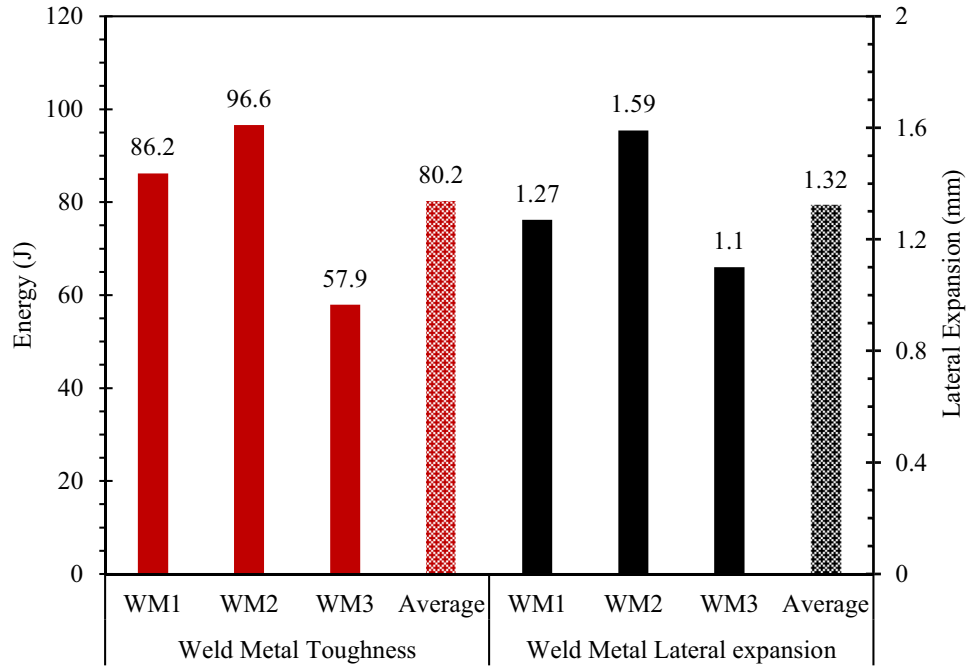
It has been reported in the work of Ghorbel et al. [24] that one of the significant outcomes of these tensile tests is that the two specimens were fractured out of the welded joint area (i.e. failure is localized in the BM). This result

Table 5 Monotonic tensile properties of the welded clad material at room temperature [24]

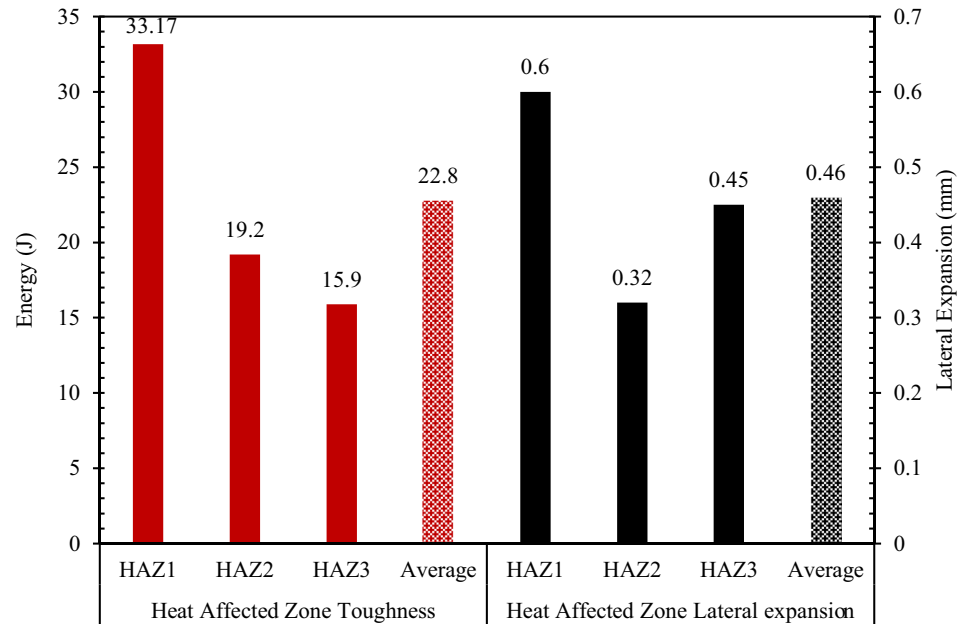
Tensile strength R_m (MPa)	487 ± 2.8
Yield Strength R_e (%)	423 ± 2.5
Elongation A (%)	31.4 ± 1.4

shows that the weld zone is more resistant than the base material, which complies with the ASME IX requirement. In addition, bending tests, applied on the four side bend specimens [24], indicated that no separations, fractures or tearing was observed on all bent surfaces which is in accordance with the industrial code ASME IX [25]. However, the bulging phenomenon, which appeared in the weld area after

Fig. 16 Measured Charpy V-notch energy and lateral expansion on **a** weld metal specimens and **b** heat-affected zone specimens

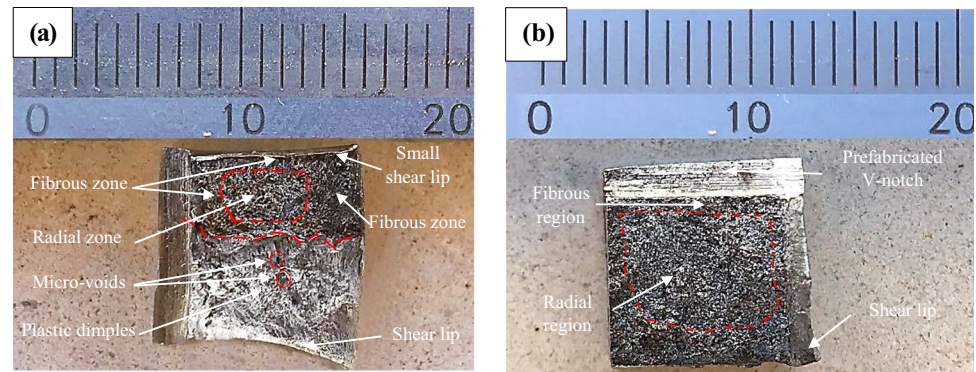


a)



b)

Fig. 17 The fractured surface observed on the impact test specimen of **a** WM and **b** HAZ



bending, was previously explained by the potential presence of a LHZ with low plasticity in the WM-TZ. Based on the previous results, the main cause producing the LHZ in the WM-TZ is the presence of a martensitic structure in which was observed microscopically and recognized by its high micro-hardness values.

3.3.3 Charpy V-notched study

Toughness tests were performed on the Charpy V-Notch specimens as shown in Fig. 3c. The main values of the WM and the HAZ toughness are plotted in Fig. 16a and b respectively. It is clearly seen that the WM toughness showed the highest values with an average of 80.2 J. However, the average of the HAZ toughness values (22.9 J) was slightly lower than the standard requirement (27 J). Herein, in order to get a coherent understanding of the obtained values, the fractured surfaces of both WM and HAZ specimens were evaluated. Figure 17 demonstrates the fractured surfaces of the Charpy impact specimens. The WM (Fig. 17a) showed two types of fracture appearances. Dimples, micro-voids and shear lips, which were induced by the shearing stress in the sliding plane, appear on the bottom of the fractured surface, while mixture of fibrous and radial zone appears on the top of the fractured surface. A small shear lip in this region can be recognised. The average value of the WM lateral expansion observed in Fig. 16a was found about 1.32 mm. It can be noted that fracture occurred by a ductile mode on the bottom and a mixed ductile and cleavage mode on the top. These findings hereby confirm the amount of energy absorbed on the WM specimens (80.2 J).

On the other hand, the optical fracture surface of the HAZ (Fig. 17b) can be divided into four parts: prefabricated V-Notch, fibrous region, radial region and shear lip. Each part is corresponding to different fracture features. The fracture initiated from the fibrous region adjacent to the prefabricated V-Notch. The surface is featured with fibrous pattern. The radial region, which located in the middle of the fractured surface, was featured with a brittle cleavage with bright and reflective facets. A small shear lip was observed

as a final rupture induced by the shearing stress in the sliding plane. The average value of the HAZ lateral expansion observed in Fig. 16b was found about 0.46 mm. It can be noted that fracture occurred by a mixture of ductile-brittle mode with predominated brittle fracture appearance. These findings hereby confirm the amount of energy absorbed on the HAZ specimens (22.9 J). It is reasonable to link the mode of the fracture toughness with the variation of micro-structure and micro-hardness. It can be noted that the ductility in the HAZ decreases due to the coarse grains observed in Fig. 10, the formation of martensitic structure and the high micro-hardness observed in Fig. 15.

4 Conclusion

In this manuscript, the structural integrity of the studied SCSP welded joint, produced by a hybrid SMAW/GTAW multi-pass welding process, was investigated through non-destructive examinations, microstructural observations and mechanical characterisation including tensile, bend, micro-hardness and impact toughness tests. As a result of this study, the following conclusions can be drawn:

- The microscopic examination carried out on the welded joint showed a typical ferritic-pearlitic structure and austenitic matrix with a dendritic δ -ferrite, which solidified in skeletal and lathy morphologies, respectively in the carbon steel and in the stainless steel weld sides. No sign of martensite was found in these investigated weld regions.
- The microscopic examination performed on the WM-TZ showed the presence of martensite laths and cellular and columnar structure characterized by their martensitic nature. It was revealed in the vicinity of the fusion boundary (FB) the presence of a decarburized layer generated by the carbon depletion from the substrate heat-affected zone (S-HAZ) during the welding process and its agglomeration along the fusion line. Despite the selection of the filler metal ER309L in the studied process, to avoid

the formation of the martensite near the BM-S/WM-TZ interface, thanks to its Ni content that acts as a diffusion barrier, type I and II boundary joints, which are characterized by their martensitic nature, were appeared.

- The micro-hardness tests showed that the highest micro-hardness values were recorded in the WM-TZ and in vicinity of the FBs with an average of 429 ± 30 HV, which confirms the presence of a martensitic structure.
- Charpy impact test results showed that the average value of the WM and the HAZ fracture toughness was 80.2J and 22.9J, respectively. The relatively low fracture energy of the HAZ was highlighted by the brittle feature of the fractured surface.
- In view of the reached outcomes, it can be retained that the main cause producing the LHZ is the martensitic structure observed in the WM-TZ along the fusion line. Martensitic structure can be avoided by adjusting the heat input parameters in such a way that the percentage of the dilution in the WM-TZ does not exceed 31% in accordance with Schaeffler diagram. The effect of the subsequent passes on the previous welded beads will be the subject of our future work.

Acknowledgements The authors would like to thank SOCOMENIN Company for their support. They equally would like to thank Mr M.T. Hbaieb and A. Badri, staff engineers at SOCOMENIN Company, for their knowledgeable help and support.

Declarations

Conflict of interest

The authors declare no competing interests.

References

1. Kaya Y, Kahraman N (2013) An investigation into the explosive welding/cladding of Grade A ship steel/AISI 316L austenitic stainless steel. *Mater Des* (1980-2015):52 367372
2. Venkateswara Rao N, Madhusudhan Reddy G, Nagarjuna S (2011) Weld overlay cladding of high strength low alloy steel with austenitic stainless steel – structure and properties. *Mater Des* 32(4):2496–2506
3. Liu BX, Yin FX, Dai XL, He JN, Fang W, Chen CX, Dong YC (2017) The tensile behaviors and fracture characteristics of stainless steel clad plates with different interfacial status. *Mater Sci Eng A* 679:172–182
4. Argade GR, Shukla S, Liu K, Mishra RS (2018) Friction stir lap welding of stainless steel and plain carbon steel to enhance corrosion properties. *J Mater Process Technol* 259:259–269
5. Ganesh P, Moitra A, Tiwari P, Sathyanarayanan S, Kumar H, Rai SK et al (2010) Fracture behavior of laser-clad joint of Stellite 21 on AISI 316L stainless steel. *Mater Sci Eng A* 527(16-17):3748–3756
6. Li C'a, Qin G, Tang Y, Zhang B, Lin S, Geng P (2020) Microstructures and mechanical properties of stainless-steel clad plate joint with diverse filler metals. *J Mater Res Technol*
7. Jing YA, Qin Y, Zang X, Shang Q, Hua S (2014) A novel reduction-bonding process to fabricate stainless steel clad plate. *J Alloys Compd* 617:688–698
8. An Q, Fan KY, Ge YF, Liu BX, Liu YC, Wang S et al (2020) Microstructure and mechanical properties of stainless-steel clad plate joints produced by TIG and MAG hybrid welding. *J Adhes Sci Technol* 34(6):670–685. <https://doi.org/10.1080/01694243.2019.1677087>
9. Chen CX, Liu MY, Liu BX, Yin FX, Dong YC, Zhang X et al (2017) Tensile shear sample design and interfacial shear strength of stainless-steel clad plate. *Fusion Eng Des* 125:431–441
10. Dhib Z, Guermazi N, Gaspérini M, Haddar N (2016) Cladding of low-carbon steel to austenitic stainless steel by hot-roll bonding: microstructure and mechanical properties before and after welding. *Mater Sci Eng A* 656:130–141
11. Tian MJ, Chen H, Zhang YK, Wang T, Zhu ZY (2015) Welding process of composite plate for construction and its welded microstructure and properties. *Heat Treat Met* 40:110–115
12. Qiu T, Wu BX, Chen QY, Chen WJ (2013) Analysis on welded joint properties of stainless clad steel plates. *Dianhanji/ Electric Welding Machine* 43(4):83–87
13. Li L, Xiao J, Han B, Zhou C, Wang X (2020) Welding L415/316L Bimetal Composite Pipe Using Post-Internal-Welding Process. *Trans Indian Inst Metals*:1–15
14. WANG W, WANG Y, LIU M, CHENG F, WU, W. (2010) Microstructure and corrosion resistance of butt joint of 1Cr18Ni9Ti+Q235 composite plate. *Transactions of the China Welding Institution* 6
15. Missori S, Murdolo F, Sili A (2004) Single-pass laser beam welding of clad steel plate. *Weld J* 83(2):65s–71s
16. Jiang W, Liu Z, Gong JM, Tu ST (2010) Numerical simulation to study the effect of repair width on residual stresses of a stainless-steel clad plate. *Int J Press Vessel Pip* 87(8):457–463. <https://doi.org/10.1016/j.ijpvp.2010.06.003>
17. Ma H, Qin GL, Geng PH et al (2015) Microstructure characterization and properties of carbon steel to stainless steel dissimilar metal joint made by friction welding. *Mater Des* 86:587–597
18. Wang SG, Dong GP, Ma QH (2009) Welding of duplex stainless steel composite plate: influence on microstructural development. *Mater Manuf Process* 24(12):1383–1388. <https://doi.org/10.1080/10426910902997456>
19. Yu WX, Liu BX, Chen CX, Liu MY, Zhang X, Fang W et al (2020) Microstructure and mechanical properties of stainless steel clad plate welding joints by different welding processes. *Sci Technol Weld Join* 25(7):571–580
20. David SA, Vitek JM (1989) Correlation between solidification parameters and weld microstructures. *Int Mater Rev* 34(1):213–245
21. David SA, Babu SS, Vitek JM (2003) Welding: solidification and microstructure. *JOM* 55(6):14–20
22. Trivedi R, David SA, Eshelman MA, Vitek JM, Babu SS, Hong T, DebRoy T (2003) In situ observations of weld pool solidification using transparent metal-analog systems. *J Appl Phys* 93(8):4885–4895
23. Bunaziv I, Olden V, Akselsen OM (2019) Metallurgical aspects in the welding of clad pipelines—a global outlook. *Appl Sci* 9(15):3118
24. Ghorbel R, Ktari A, Haddar N (2021) Experimental analysis of temperature field and distortions in multi-pass welding of stainless clad steel. *Int J Adv Manuf Technol* 113:3525–3542. <https://doi.org/10.1007/s00170-021-06788-y>
25. ASME IX (2017) ASME Boiler and Pressure Vessel Code, Section IX: Welding and Brazing Qualifications. An International Code, New York

26. Kožuh S, GOJI M (2009) Mechanical properties and microstructure of austenitic stainless steel after welding and post-weld heat treatment. *Kovove Materiari* 47:253–262
27. Nelson TW, Lippold JC, Mills MJ (1998) Investigation of boundaries and structures in dissimilar metal welds. *Sci Technol Weld Join* 3(5):249–255
28. Ming H, Zhang Z, Wang J, Han EH, Ke W (2014) Microstructural characterization of an SA508–309L/308L–316L domestic dissimilar metal welded safe-end joint. *Mater Charact* 97:101–115. <https://doi.org/10.1016/j.matchar.2014.08.023>
29. Feng Y, Luo Z, Liu Z, Li Y, Luo Y, Huang Y (2015) Keyhole gas tungsten arc welding of AISI 316L stainless steel. *Mater Des* 85:24–31
30. Chassignole B (2000) Influence de la structure métallurgique des soudures en acier inoxydable austénitique sur le contrôle non destructif par ultrasons (Doctoral dissertation, Lyon, INSA)
31. Dhib Z, Guermazi N, Ktari A, Gasperini M, Haddar N (2017) Mechanical bonding properties and interfacial morphologies of austenitic stainless steel clad plates. *Mater Sci Eng A* 696:374–386
32. Li K, Li D, Liu D, Pei G, Sun L (2015) Microstructure evolution and mechanical properties of multiple-layer laser cladding coating of 308L stainless steel. *Appl Surf Sci* 340:143–150
33. Rathod DW, Pandey S, Aravindan S, Singh PK (2016) Diffusion control and metallurgical behavior of successive buttering on sa508 steel using Ni–Fe alloy and inconel 182. *Metallogr Microstruct Anal* 5(5):450–460
34. Kou S (2003) *Welding metallurgy*. USA, New Jersey, pp 431–446
35. Wu Y, Patchett BM (1992) Formation of crack-susceptible structures of weld overlay of corrosion resistant alloys. *Materials Performance: Sulphur and Energy*, pp 283–295
36. Nelson TW, Lippold JC, Mills MJ (1999) Nature and evolution of the fusion boundary in ferritic-austenitic dissimilar weld metals, Part 1-Nucleation and growth. *Weld J-New York* 78:329–s
37. Rowe MD, Nelson TW, Lippold JC (1999) Hydrogen-induced crackwing along the fusion boundary of dissimilar metal welds. *Weld J-New York* 78:31–s
38. Nelson TW, Lippold JC, Mills MJ (2000) Nature and evolution of the fusion boundary in ferritic-austenitic dissimilar metal welds—part 2: on-cooling transformations. *Weld Res* 10:267–277

Publisher's note Springer Nature remains neutral with regard to jurisdictional claims in published maps and institutional affiliations.